Research Article | Vol. 29, No. 24 / 22 Nov 2021 / Optics Express 39904

Optics EXPRESS

Optical module for single-shot quantitative phase imaging based on the transport of intensity equation with field of view multiplexing

JOSE ANGEL PICAZO-BUENO* AND VICENTE MICÓ

Departamento de Óptica y de Optometría y Ciencias de la Visión, Universidad de Valencia, C/ Doctor Moliner 50, Burjassot 46100, Spain
*j.angel.picazo@uv.es

Abstract: We present a cost-effective, simple, and robust method that enables single-shot quantitative phase imaging (QPI) based on the transport of intensity equation (TIE) using an add-on optical module that can be assembled into the exit port of any regular microscope. The module integrates a beamsplitter (BS) cube (placed in a non-conventional way) for duplicating the output image onto the digital sensor (field of view – FOV – multiplexing), a Stokes lens (SL) for astigmatism compensation (introduced by the BS cube), and an optical quality glass plate over one of the FOV halves for defocusing generation (needed for single-shot TIE algorithm). Altogether, the system provides two laterally separated intensity images that are simultaneously recorded and slightly defocused one to each other, thus enabling accurate QPI by conventional TIE-based algorithms in a single snapshot. The proposed optical module is first calibrated for defining the configuration providing best QPI performance and, second, experimentally validated by using different phase samples (static and dynamic ones). The proposed configuration might be integrated in a compact three-dimensional (3D) printed module and coupled to any conventional microscope for QPI of dynamic transparent samples.

1. Introduction

Many microscopic objects of interest, such as biological cells, are essentially transparent meaning that they do not absorb the light passing through them, thus making their observation and analysis cumbersome with a traditional bright-field microscope. Despite such objects do not modify the amplitude of the light, they present internal structures with different refractive indices (RI) that introduce phase delays in the wavefront of the illumination. Those phase changes can be converted into intensity variations with, for example, Zernike phase contrast [1] and Differential Interference Contrast [2] microscopy techniques. Although those techniques were significant in the advancement of microscopy and there are nowadays quantitative versions of them [3–6], they do not provide quantitative information of the phase, so that relevant characteristic of the samples such as thickness and RI cannot be quantified.

Quantitative phase imaging (QPI) can be achieved by diverse techniques based on different basic principles [7–9] but probably the most well-established one is based on interferometry applied to digital microscopy [10–12]. In digital holographic microscopy, an external reference beam is coherently superimposed with the original object beam forming an interferogram, and the phase information is retrieved by using different types of numerical reconstruction algorithms [12]. However, they normally require a high degree of coherence of the light source (suffering of coherent noise), the separation and combination of the object and reference beams (sophisticated interferometric configuration and sensitive to external disturbances), and a phase unwrapping algorithm (computationally demanding), factors that may limit their usability in biological and medical science [9].

#439047 https://doi.org/10.1364/OE.439047
Journal © 2021 Received 1 Aug 2021; revised 18 Oct 2021; accepted 18 Oct 2021; published 16 Nov 2021

Optics EXPRESS

Alternatively, there exist non-interferometric techniques alleviating some of those drawbacks. Inside this category, we can distinguish between wavefront sensing techniques [13,14], iterative phase retrieval approaches [15–17], and deterministic phase retrieval techniques [9,18,19]. On one hand, wavefront sensing techniques employ special types of sensors for phase detection, such as Shack-Hartmann [13], or pyramid [14] wavefront sensors. However, they are seldom used for QPI since they limit the spatial resolution of the recovered wavefront. On the other hand, iterative phase retrieval approaches, such as Gerchberg-Saxton [15] or ptychography [16,17], utilize several intensity measurements and impose some constraints in order to iteratively recover the phase distribution. But iterative algorithms often require a large amount of intensity data and a high number of iterations to obtain a trustworthy solution, thus restricting their use for high-speed and real-time imaging applications. And finally, deterministic phase retrieval techniques aim to extract the phase from intensity distributions as a mathematical "inverse problem", but in a non-iterative way through deterministic algorithms. One example of those methods is quantitative differential phase contrast (DPC) [20–22]. DPC uses a pair of images with complementary asymmetric illumination patterns for QPI. Another deterministic method is based on the solution of the transport of intensity equation (TIE).

TIE is a second-order elliptic partial differential equation, which essentially provides a quantitative relation between the phase at a given propagation plane and the axial intensity derivative around such a plane [18]. Hence, the phase distribution of the light diffracted by phase samples can be directly determined from two or more slightly defocused intensity images by solving the TIE without iterative operations [9]. TIE was first derived from the conservation of energy on propagation (Helmholtz equation) under paraxial approximation by Teague in 1982 [23]. Concerning its applicability to QPI in optical microscopy, in 1984, Streibl [24] realized that TIE could be applied for phase imaging in optical microscopy by demonstrating the effect of phase gradient enhancement by taking the axial intensity derivative. In 1998, Paganin and Nugent reinterpreted the meaning of "phase" of partially coherent fields [19], which allowed the researchers in QPI the employment of low-coherence light sources for improving the resolution and image quality. In the same year, Barty *et al.* reported the first TIE-based QPI results of cheek cells and optical fibers [25]. Since then, TIE phase retrieval methods have found many applications in QPI [9]. For instance, TIE was successfully applied to the quantitative analysis of phase and RI of optical fibers and other technical phase objects [26–29], for quantitative detection of the morphology and growth rate of cells [30,31], for imaging contrast enhancement of unstained cells under microbeam irradiations [32], and for quantitative measurement of the birefringence effect of unstained isolated cardiomyocytes [33], just to cite some examples.

TIE requires the acquisition of two or more defocused images of the sample, which are conventionally captured at different time lapses, either moving axially the camera or the object using manual adjustment or mechanical devices. Consequently, the data acquisition speed is inevitably slowed down and thereby restricts its applicability to static objects (static at least during the total recording time). This fact severely limits the application of TIE methods when dealing with dynamic phase samples as well as it imposes severe requirements concerning mechanical and thermal stability in the system. But in the last decade, high-speed and single-shot QPI based on TIE has been successfully reached by implementing different advanced optical configurations and strategies, which enable the through-focus intensity recording without mechanical motion. Thus, Waller *et al.* implemented in 2010 a volume holographic microscope to simultaneously record two or more laterally separated and defocused images [34], and also demonstrated that the chromatic aberrations of poor quality microscope lenses can also be utilized to obtain slightly defocus images suitable for single-shot TIE application [35]. Two years later, Gorthi and Schonbrun reported a TIE technique based on flow cytometry where the acquisition of through-focus intensity images was performed by vertically tilting the microfluidic channel [36]. In 2013, Zuo *et al.* attached a 4*f* optical system to the output port of a conventional bright-field

Optics EXPRESS

microscope including either an electronically tunable lens [37] or a Michelson-like architecture with a spatial light modulator (SLM) [38] for high-speed sequential and single-shot intensity acquisition, respectively. In the same year, Di Martino *et al.* employed a beam splitter and several mirrors to define a TIE setup to simultaneously record two defocused and laterally separated images [39]. In 2016, Tian *et al.* attached two identical digital sensors at the binocular tubes of a commercial microscope to capture the same field of view (FOV) but at different focal planes [40]. In addition, Yu *et al.* used a SLM in a 4*f* system to provide three slightly defocused and laterally shifted intensity images [41], whereas Yang and Zhan integrated a module, including a distorted grating, with a smartphone camera to achieve single-shot QPI from two defocused images [42]. In 2018, Li *et al.* designed a flipping Michelson-like module including a retro reflector to provide the two lateral and defocused images [43]. And Zhou reported a single-shot TIE technique in which intensity distributions were recovered from the digital propagation of a digital inline hologram [44]. In 2020, Gupta *et al.* proposed a cost-effective setup consisting of a 4*f* optical system and a Michelson architecture with tilted mirrors for TIE-based single-shot QPI [45]. Furthermore, Nomura *et al.* employed a parallel optical glass and an iris to provide two defocused and laterally separated images [46]. In addition, Zhang *et al.* employed the bifocal property of a Greek-ladder sieve to implement a single-shot common-path TIE method [47]. In 2021, Engay *et al.* have reported the use of a polarization-dependent all-dielectric metasurface utilized to simultaneously record two defocused images with orthogonal polarizations [48]. Moreover, Yoneda *et al.* have used a computer-generated hologram technique to simultaneously record multiple defocused intensity distributions, allowing higher-order approximation of the axial intensity derivate and thus improving the image quality of single-shot TIE-based QPI [49]. Finally, Chen *et al.* have achieved single-shot QPI from two defocused images by connecting, at the microscope side port, a compact 3-D printed module consisting of a beam splitter and a board-level camera with two CMOS imaging chips [50].

Following this trend of single-shot QPI TIE-based approaches, we report here on a novel low-cost, simple, and robust module and method for non-interferometric, non-iterative, and single-shot QPI based on TIE approach. The layout is inspired by the holographic add-on module recently reported in [51] and it consists on a beam splitter cube, a Stoke lens and an optical glass plate attached to a digital sensor. The proposed system provides, at the same time, two laterally separated intensity images with slight negative- and positive-defocus around the image plane, where the phase can be easily extracted by solving TIE algorithms. A complete analysis of the system performance is presented in Section 2. Furthermore, the feasibility of the system for QPI is experimentally demonstrated involving different static and dynamic phase samples (see Section 3). Finally, Section 4 includes a discussion and concludes the paper.

2. System analysis

2.1. Layout description

The proposed optical layout for validating our single-shot QPI method based on TIE with field of view (FOV) multiplexing is presented in Fig. 1. It is integrated by two parts: a conventional microscope configuration (objective + tube lens) working in infinity configuration and the optical module for TIE-based QPI using a single snapshot. Hence, the sample is illuminated in a transmission mode with a LED light source and the microscope embodiment produces an image of the sample at the image focal plane of the TL where a digital sensor is placed. But before reaching the sensor, light is passing through the proposed TIE-based optical module composed by a Stokes lens (SL), a beam splitter cube (BSC) and an optical glass (OG) plate. In more detail, the BSC generates two side-by-side replicas of the image due to its unconventional arrangement: it is placed (see Fig. 1) in such a way that its semireflecting layer becomes parallel to the optical axis of the microscope. Furthermore, the BSC is laterally shifted, so that the light is only transmitted by one half, leaving unused the other one. In this position, the BSC provides two inverted

Optics EXPRESS

replicas of the image delivered by the microscope embodiment. Since the BSC is mounted onto a tilting platform including different adjusting screws, the semireflecting layer of the BSC can be accurately aligned to the optical axis. That ensures the replicas are not overlapping each other while appearing symmetrically and maximally filling the camera sensor area. Note also that the digital sensor is also laterally shifted from the optical axis to allow this side-by-side image matching.

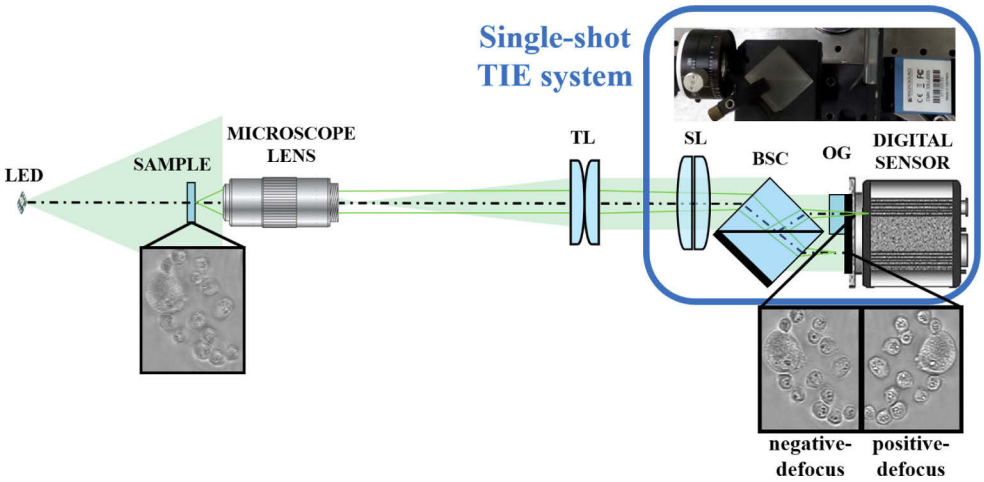

Fig. 1. Optical scheme of the proposed experimental setup for the proposed method including a picture of the TIE-based add-on module (blue rectangle with rounded corners) where the different elements are easily identified. The figure includes some experimental results concerning prostate cancer cells that are essentially transparent at the sample plane and can be visualized with negative- (left) and positive- (right) defocus at the multiplexed FOV provided by the digital sensor.

However, this BSC arrangement introduces some aberrations that are critical to be compensated for high-quality imaging [51,52]. More concretely, it introduces a significant amount of prismatic effect and astigmatism in a similar case than a tilted plane-parallel plate does. The prismatic effect can be easily compensated by moving the sample in the transverse plane but mitigation of the astigmatism requires a more complex device/procedure, such as specially designed optical components [53,54] or digital procedures [55]. For such an astigmatism compensation, we use a labmade SL consisting in two pure cylindrical lenses of equal but opposite dioptric powers. Such lenses are mounted onto a Risley prism mount, so that the lenses can be rotated not only one to each other but also globally to change both the astigmatic power and its orientation. A more detailed description and analysis of such a SL is given in [51].

Hence, the combination SL - BSC generates two inverted intensity images with compensated astigmatism at the same axial distance, that is, with the same defocus condition, and they are not still suitable for axial intensity derivative calculation. For that purpose, we must induce a slight axial separation (or defocus) between replicas. Here, this is achieved with the inclusion of an OG plate within the optical path of one of the images (see Fig. 1). Such an OG is basically a plane-parallel plate that moves backwards the image plane of the corresponding replica by a given distance that depends on its geometrical properties (we will be back to this in next section). And in order to properly apply the single-shot TIE algorithm, the digital sensor is axially placed halfway between the two focusing planes of the replicas to simultaneously acquire both the negative- and positive-defocused intensity images required for intensity derivative estimation.

Optics EXPRESS

2.2. Axial defocusing distance induced by the optical glass plate

The presence of a plane parallel OG plate at the image space introduces an axial displacement Δz of the image according to the expression,

$$\Delta z = d\left(1 - \frac{1}{n}\right) \tag{1}$$

being d and n the thickness and RI of the OG, respectively. Thus, there is a linear relationship between Δz and d. In that way, the axial defocusing can be easily and accurately changed by modifying the thickness of the OG plate.

In addition, we can calculate the equivalent axial shift Δz in the object space as a function of d. For that, we must consider the connection between the object and image axial dimensions, which can be found by solving the coupled lens system equations in our infinity corrected microscope layout,

$$\Delta z = -\frac{f_T^2}{f_0^2 + (f_T + f_0 - L)\delta z}\delta z \tag{2}$$

Here f_O and f_T are the focal lengths of the microscope lens and the TL, respectively, and L is the tube length. The negative sign in Eq. (2) indicates that when the sample moves towards the objective, the image moves away from the TL, and vice versa. In our case, Δz will be in the order of microns, whereas the quantities f_O, f_T and L will be several hundreds of millimeters, so we can state that $\Delta z \ll f_T, f_O, L$, and therefore $f_O^2 \gg \delta z(f_T + f_O - L)$. Hence, the term $\Delta z(f_T + f_O - L)$ can be neglected and the relation between the object and image displacements becomes,

$$\Delta z = -\left(\frac{f_T}{f_0}\right)^2 \delta z = -M^2 \delta z \tag{3}$$

where M is the lateral magnification of the imaging system, which in an infinity corrected optical configuration is given by $M = \frac{f_T}{f_O}$.

Finally, combining Eqs. (1) and (3), we achieve a linear relationship between Δz and d in the form

$$\delta z = -\frac{d}{M^2}\left(1 - \frac{1}{n}\right) \tag{4}$$

Hence, an increment in the thickness of the OG plate will be related to an effective approach of the object towards the microscope lens, according to Eq. (4).

2.3. TIE-based phase retrieval algorithm

The TIE can be derived from the paraxial wave equation as Teague demonstrated in [18,23]. Considering an optical field with a complex amplitude being $O(x, y, z) = \sqrt{I(x, y, z)} \cdot e^{i\varphi(x,y,z)}$ propagating along z-axis, then the TIE can be mathematically expressed as

$$\nabla(I_Z(x, y) \bullet \nabla\phi_Z(x, y)) = -\frac{2\pi}{\lambda}\frac{\partial I(x, y, z)}{\partial z} \tag{5}$$

where λ is the wavelength of the light source, ∇ is the gradient operator in the transverse plane (x, y), and $I_z(x, y)$ and $\phi_z(x, y)$ are the intensity and phase distributions at a particular plane z, respectively. Equation (5) means that the phase distribution at the propagation distance z can be determined by recording a set of intensity images at slightly different planes [56].

In the particular case of weak absorption (phase) objects under uniform illumination, the intensity at the image plane may be regarded as nearly constant in the transverse plane, that

Optics EXPRESS

is, $I_z(x,y) = I_z \approx const.$, and then Eq. (5) can be simplified to a two-dimensional (2D) Poisson equation in the form,

$$\nabla^2 \phi_Z(x,y) = -\frac{2\pi}{\lambda I_Z}\frac{\partial I(x,y,z)}{\partial z} \tag{6}$$

Hence, the phase distribution may then be directly extracted from Eq. (6) as

$$\phi_Z(x,y) = -\frac{2\pi}{\lambda I_Z}\nabla^{-2}\left(\frac{\partial I(x,y,z)}{\partial z}\right) \tag{7}$$

where ∇^{-2} is the inverse Laplacian operator. Considering that such an operator can be efficiently implemented with the differential properties of the Fourier transform [56,57], the phase distribution can be rapidly calculated by using 2D fast Fourier transform (FFT) algorithm,

$$\phi_Z(x,y) = -\frac{2\pi}{\lambda I_Z} FFT^{-1}\left[\frac{1}{4\pi^2(u^2+v^2)} FFT\left[\frac{\partial I(x,y,z)}{\partial z}\right]\right] \tag{8}$$

Here, u and v are the spatial frequencies corresponding to x and y axis, respectively. It is important to note that Eq. (8) has a singularity (pole) at $u = v = 0$. Nonetheless, such a singularity can be easily avoided by employing a Tikhonov regularization, which is also used to remove very low frequency artifacts [58–60]. Hence, the final expression for the phase distribution becomes,

$$\phi_Z(x,y) = -\frac{2\pi}{\lambda I_Z} FFT^{-1}\left[\frac{(u^2+v^2)}{4\pi^2[(u^2+v^2)+\gamma]} FFT\left[\frac{\partial I(x,y,z)}{\partial z}\right]\right] \tag{9}$$

being γ the regularization parameter [60], whose value can be directly calculated from the physical dimensions X and Y of the image as $\gamma = (\max(X,Y))^{-1}$. Finally, the axial intensity derivative $\partial I(x,y,z)/\partial z$ can be experimentally estimated with the acquisition of the intensity in two planes separated $\Delta z/2$ either side of the plane of interest and by the central finite-difference formula [61] as

$$\frac{\partial I(x,y,z)}{\partial z} \approx \frac{I(x,y,+\Delta z/2) - I(x,y,-\Delta z/2)}{\Delta z} \tag{10}$$

Equation (10) is more accurate when smaller the distance Δz is. This central difference could provide a more accurate estimation of the intensity derivative as well as a better tolerance of the spatial incoherence of the illumination [38,62].

3. Experimental implementation

In this section, we present the experimental validation of our single-shot TIE-based optical system for QPI. In the experiments, we have used the green emission light (522.5–525 nm wavelength) of a RGB LED (Adafruit, model SK6812) as illumination light source. The sample is placed onto a translation stage with micrometer movement for precise displacement. As optics, we have employed a microscope system involving a 10X/0.30NA infinity corrected microscope lens and a tube lens with $\boldsymbol{f_T} = 200$ mm, which provides a lateral magnification and resolution of $\boldsymbol{M} = 11$X and $\boldsymbol{\rho} = 1.44$ µm, respectively. The replicas of the image are provided by a non-polarizing BSC (25.4 mm side), whereas the axial defocusing between the replicas is achieved by using a set of microscope slides as the OG plates. The microscope slides have a thickness of 1 mm and are made of crown glass (BK7), which presents a RI of $\boldsymbol{n} = 1.52$ at the illumination wavelength $\boldsymbol{\lambda} = 525$ nm. Finally, the intensity images are recorded with a monochrome CMOS sensor (Imaging Source, model DMK 33UJ003, 3856 × 2764 pixels, 1.67 µm pixel size, 14 fps).

Optics EXPRESS

3.1. System performance: analysis of the fine adjustment between replicas

The process of adding the different elements in our optical module is illustrated through Fig. 2 for the case of a chrome on glass USAF resolution test target. Figure 2(a) shows the intensity image provided by the microscope before including the TIE-based module. Once the BSC is introduced, Fig. 2(b) includes the two replicas of the USAF test target that are significantly distorted by astigmatism as we can easily see since the horizontal bars appear in focus but not the vertical ones. We have measured a total amount of astigmatism equivalent to 0.84D (in cylindrical notation), which is big enough to destroy the image quality in a microscope, especially for the smallest details (close to the resolution limit). For compensating the astigmatism, the SL is inserted into the system and manually tuned to its best position (see Fig. 2(c)). After that, we include the OG plate into the system to modify the optical path of the left part of the image. Finally, the CMOS camera is placed halfway between both imaging planes to simultaneously record the negative- and positive-defocused intensity distributions, presented at the left and right part of Fig. 2(d), respectively. In all images, the central parts included in the rectangles are magnified for improving visualization.

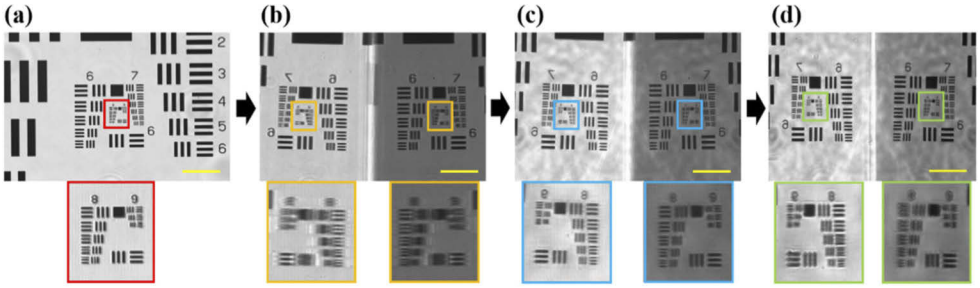

Fig. 2. Recording sequence in the proposed single-shot TIE-based layout: (a) direct image without the TIE-based system, (b) astigmatic image provided by the BSC, (c) astigmatic-free image including the SL, and (d) final image after OG plate inclusion and CMOS positioning between image planes. Yellow scale bars are 100 μm.

Once both image replicas of the input object are digitally captured in a single snapshot, the phase retrieval algorithm proceeds as follows. First, a normalization process is needed since the two defocused replicas present different background intensities [43]. That is due to both the splitting ratio of the BSC is not exactly 0.5:0.5 and the reflection and absorption of the OG plate. This process is carried out by recording an additional image of the background intensity without the sample. Then the object image $I_{obj}(x, y)$ containing both defocused replicas is normalized by the background image $I_{back}(x, y)$, giving a normalized image in the way $I_{norm}(x, y) = I_{obj}(x, y)/(I_{back}(x, y) + \varepsilon)$, with $\varepsilon = 10^{-6}$ being a regularization parameter to avoid division-by-zero instability. Thus, such a process provides not only an equalization of the intensity but also the removal of the background inhomogeneities coming from dust and imperfections and spurious diffraction effects caused by the semireflecting layer of the BSC in the middle region of the image. After normalization, the defocused replicas $I(x, y, -\Delta z/2)$ and $I(x, y, \Delta z/2)$ are separately extracted from $I_{norm}(x, y)$ by spatial filtering them out. And these two images must be combined one with the other having the best accuracy possible since the better the adjustment between replicas, the more accurate the phase retrieval process [40].

For fine matching both replicas, a calibration process based on image-processing is defined using a high-resolution chrome on glass USAF target (Edmund Optics). This process needs only to be done once in a calibration preliminary stage and does not need to be implemented every time the method is going to be used. In this digital preprocessing stage, we compute the maximum of the 2D cross correlation between replicas involving both 2D lateral translation and

Optics EXPRESS

rotation. Since both $I(x, y, -\Delta z/2)$ and $I(x, y, \Delta z/2)$ are assumed to be defocused by the same (but inverted) distance, and thus having opposite intensity contrast, we can invert the contrast of one replica in order to enhance the performance of the adjustment process. In addition, it is also worth it to point out that the fitting process is more efficient when involving absorptive objects instead of transparent ones, since amplitude objects present more contrast in intensity images than phase objects. Once the images are perfectly fitted in rotation and lateral translation, the axial intensity derivative is numerically estimated using Eq. (10). Finally, the phase distribution is recovered from Eq. (9), and assuming that the intensity I_z at the image plane in the case of pure phase objects can be obtained by averaging the two defocused images as $I_z = mean\left(\frac{I(x,y,-\Delta z/2)+I(x,y,\Delta z/2)}{2}\right)$ [38,63].

Figure 3 illustrates the previously described process concerning phase retrieval using a USAF-type phase resolution test target from Benchmark Technologies (200 nm theoretical feature height) and considering an OG plate with $d = 4$ mm. The whole object and normalized intensity images are included in Figs. 3(a) and 3(b), respectively, while Figs. 3(c) and 3(d) present the negative- (left) and positive- (right) defocused replicas after spatial fitting process, respectively. Finally, Figs. 3(e) and 3(f) show the axial intensity derivative and the recovered phase distribution reached by our proposed single-shot QPI TIE-based approach, respectively.

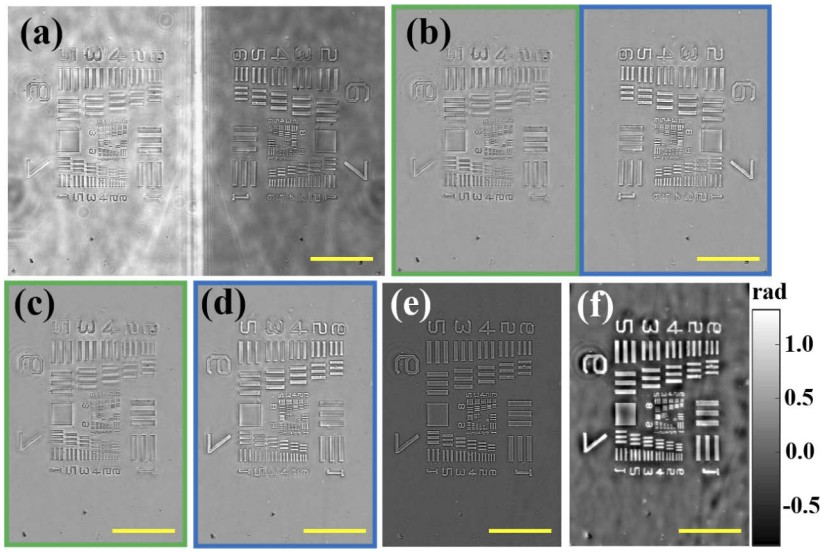

Fig. 3. Phase retrieval procedure. (a) recorded intensity image, (b) normalized image after background subtraction, (c) negative- and (d) positive-defocused replicas, (e) axial intensity derivative estimation, and (f) reconstructed phase distribution. Yellow scale bars are 100 μm.

3.2. System performance: defocus calibration

The two-plane-based finite difference formula given by Eq. (10) is simple and easy to implement for axial derivative intensity estimation. However, it presents the problem of the correct selection of Δz (the defocus distance), which must be neither too small nor too large to have an acceptable quality in the phase reconstructions [18,61,64]. On one hand, a too small Δz provides accurate derivative estimation and improved spatial resolution, but the signal-to-noise ratio (SNR) is compromised by the presence of noise [61]. On the other hand, a too large Δz reduces the noise and ensures an adequate level of SNR, but the linear derivative assumption is compromised

Optics EXPRESS

and appear non-linearity errors that deteriorate the spatial resolution, thus "blurring" the phase images [65].

Hence, we must choose an appropriate defocus distance Δz in order to optimize both the accuracy of the derivative estimation and the quality of the phase reconstructions [9]. To do so, we analyze two parameters which usually give an idea of the quality of the images: the spatial resolution and the spatial noise. Those parameters are computed in the quantitative phase images provided by our TIE-based system for the case of the USAF-type phase resolution target (200 nm theoretical height) at 10 different Δz values. In our case, Δz can be changed by modifying the thickness d of the OG plate according to Eq. (1), which is easily achieved by adding or removing microscopes slides in the layout at steps of 1 mm. We have performed the defocus distance analysis for the interval between $d =$ [1,10] mm or, equivalently, $\Delta z =$ [0.34, 3.4] mm, which is broad enough to appreciate the previously mentioned effects (lateral resolution and background noise). Figure 4 presents the experimental results, including the quantitative phase images obtained when $d = 1$, 4, and 10 mm [see Figs. 4(a), 4(b), and 4(c) respectively], as well as the dependence of such two parameters with d [included at Fig. 4(d)]. The background noise is measured for every retrieved phase image by computing the standard deviation (STD) values at the regions enclosed in the dotted red rectangles included in Fig. 4(a).

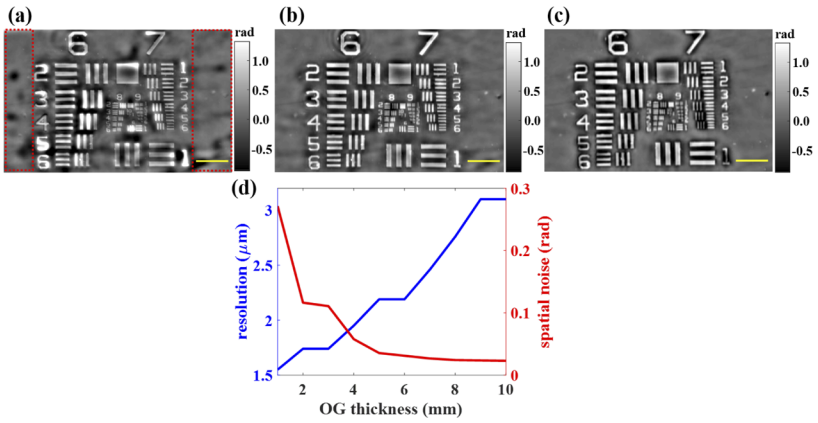

Fig. 4. Defocus distance optimization involving a phase resolution test target. (a), (b), and (c) recovered phase distributions for $d = 1$, 4, and 10 mm, respectively. (d) Quantitative relation of the lateral resolution and spatial phase noise with d. Yellow scale bars are 50 μm.

Looking at Fig. 4, we can qualitatively [see Figs. 4(a), 4(b), and 4(c)] and quantitatively [see Fig. 4(d)] appreciate how the background noise of the retrieved phase images decreases as defocus distance increase, whereas the spatial resolution improves with a diminution of such distance. Thus, a well-balanced reconstruction image is reached when an optimum compromise between noise and resolution is obtained that, in our case, seems to be at $d = 4$ mm or, equivalently, $\Delta z = 1.37$ mm where the noise is significantly dropped by almost 80% [STD values from 0.27 ($d = 1$ mm) to 0.06 rad ($d = 4$ mm)] and the spatial resolution is only reduced in a 20% (from 1.55 to 1.95 μm). Notice that, according to Fig. 4(d), one can select either a smaller or larger d in case of requiring either better resolution or better SNR, respectively.

In order to reinforce our defocus distance analysis, we have considered the phase accuracy as another important figure to be studied. For that, we have analyzed the phase steps introduced by the different elements conforming the thinnest USAF-type test of the quantitative phase target, having a nominal thickness of 50 nm and an estimated thickness of 56.6 nm (estimation based on mean of measured targets from the same master substrate according to manufacturer data). In this case, we have computed both the mean and STD values of the phase steps as a function of

Optics EXPRESS

the defocus distance, represented in the form of the OG thickness, and the values are included in Table 1.

Table 1. Phase accuracy analysis as a function of the defocus distance for the case of an USAF-type phase target with 50 nm thickness

OG thickness (mm)	1	2	3	4	5	6	7	8	9	10
Mean value (rad)	0.55	0.40	0.38	0.34	0.33	0.31	0.31	0.30	0.30	0.29
STD (rad)	0.16	0.08	0.08	0.04	0.04	0.04	0.03	0.02	0.02	0.02

To validate these phase values, we must compare them with the values computed from the thickness values $t(x, y)$ provided by the manufacturer. These phase values are calculated with the following expression,

$$\phi(x, y) = \frac{2\pi}{\lambda}(n_{obj}(x, y) - n_{med}(x, y)) \cdot t(x, y) \tag{11}$$

where $n_{obj}(x, y)$ and $n_{med}(x, y)$ are the RI distributions of the object and the surrounding medium, respectively. In this case, the target material of the quantitative phase target is an acrylate polymer on Corning Eagle XG Glass, having a constant RI of $n_{obj}(x, y) = n_{obj} = 1.513$ for the used illumination wavelength, and the surrounding medium is air with a constant RI of $n_{med}(x, y) = n_{med} = 1$. Hence, the elements of the USAF-type phase target should introduce a phase delay of $\phi_{nom} = 0.31$ or $\phi_{est} = 0.35$ rad, according to nominal ($t_{nom} = 50$ nm) and estimated ($t_{est} = 56.6$ nm) thickness values provided by the manufacturer, respectively. Looking at the Table 1, we can see how phase values start to stabilize from $d = 4$ mm in terms of STD, presenting a similar behavior than the spatial phase noise plotted in Fig. 4(d). In addition, only the mean values of the phase steps computed in the range of $d = 4$ - 7 mm are enclosed in the interval defined by the manufacturer $\phi = [0.31, 0.35]$ rad, being the case of $d = 4$ mm which provides the closest phase step value to the estimated by the manufacturer.

3.3. Experimental validation from a quantitative point of view

Once the proposed system is fine tuned up, experimental validation of our TIE-based for QPI is compared with classical TIE method implemented from two defocused intensity images recorded in time sequence and considering Eqs. (9) and (10). To allow this, we introduce a mirror between the TL and the SL in order to redirect the light at 90 degrees towards an identical digital sensor, which records the defocused images sequentially in time by moving the object axially forward or backward the object plane. The axial defocus distances $\Delta z/2$ are calculated from Eq. (4), which for a $d = 4$ mm gives a $|\delta z| = 11.3$ µm, so that the object is moved to the planes $\pm\delta z/2 = \mp 5.7$µm. Figure 5 includes the experimental results achieved by both methods involving the USAF-type phase resolution target (200 nm theoretical height). The results are partially organized in rows and columns as follows: rows (1) and (2) include the images provided by our system and by classical TIE, respectively, while columns (a) and (b) show the negative- and positive-defocused intensity images after spatially fitting process; finally, column (c) presents the retrieved quantitative phase images that present similar phase values. Notice that the background of the phase image provided by our method is not as homogeneous as in the case of the classical TIE phase image (see Figs. 5(c1) and 5(c2), respectively). That may be mainly due to the presence of residual dirt on the optical surfaces of the different elements comprising the optical module.

In addition, we have performed a plot along red and blue lines included in Figs. 5(c1) and (c2) to directly compare the thickness profiles achieved by both methods [see Fig. 5(d)]. Such thickness distributions $t(x, y)$ can be calculated from the phase values in a straightforward way considering the Eq. (11). Looking at Fig. 5(d), we can notice a good agreement between the thickness values achieved by both methods. Finally, according to the manufacturer, such

Optics EXPRESS

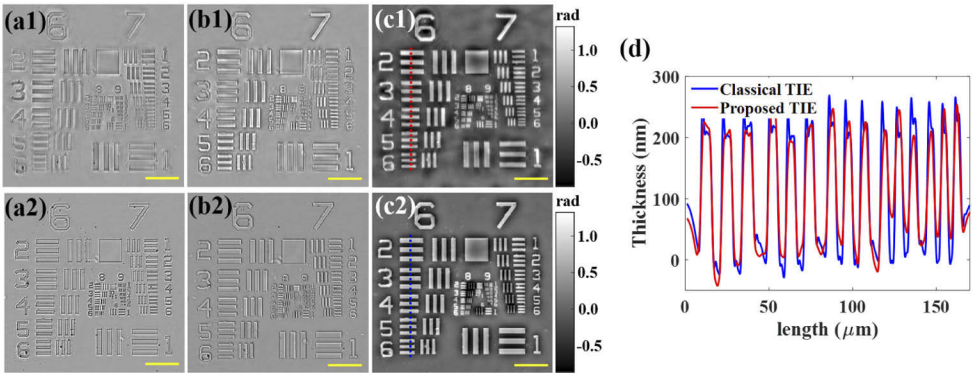

Fig. 5. Experimental validation of our proposed TIE-based system for QPI involving an USAF phase resolution test target. Rows (1) and (2): results coming from our system and classical TIE, respectively. Columns (a), (b), and (c): negative-defocused, positive-defocused, and quantitative phase images, respectively. (d) Comparative thickness plot computed from phase images along red and blue dotted lines included in (c1) and (c2). Yellow scale bars are 50 μm.

structures have a nominal theoretical thickness of 200 nm and an estimated thickness of 222.5 nm, which present high concordance with the experimental values, thus validating our approach for QPI.

Once validated for QPI, we now demonstrate that our approach can properly obtain thickness profiles of elements requiring higher sensitivity. In this case, we have achieved the thickness profiles, using our approach, of the thinnest USAF-type phase targets (50, 100, and 150 nm theoretical height) by following the same procedure as before. Figure 6 shows the thickness profiles computed along the same elements considered in Fig. 5(d) in a color-coded form, that is, red, blue, and green lines correspond to 50, 100, and 150 nm, respectively. In Fig. 6, we have also included both the nominal (lower color-coded dashed lines) and estimated (upper color-coded dashed lines) thickness values provided by the manufacturer. Here, we can clearly see how the thickness profiles are in good agreement with the interval defined between nominal and measured values, even in the case of the smallest thickness (50 nm). Hence, we can state that our approach can perfectly quantify thicknesses of, at least, a tenth of the illumination wavelength.

3.4. Experimental validation for static biosamples

After fine tuning calibration and quantitative phase validation using test targets, our system is validated with different lines (PC-3, LnCaP and RWPE-1) of prostate cancer cells. Such cells were cultured, at standard cell culture conditions (in a humidified incubator with 5% CO_2 at 37°C), in RPMI 1640 medium with 10% fetal bovine serum, 100U/ml Penincillin and 0.1 μg/ml Streptomycine. After the cells reached to a confluent stage, they were released from the culture support and centrifuged. By centrifugation, the supernatant fluid was discarded, and the cells were resuspended in a cytopreservative solution and fixed in a microscope slide. Figure 7 presents the experimental results in different rows and columns. On one hand, each row corresponds to a different cell line. Thus, LNCAP, PC-3, and RWPE-1 cells are included in the upper (labelled as 1), central (labelled as 2) and lower (labelled as 3) rows, respectively. On the other hand, different columns present: (a) the whole normalized intensity image, (b) the axial intensity derivative estimation of the region enclosed in yellow rectangle in (a), and (c) the retrieved quantitative phase distribution.

Optics EXPRESS

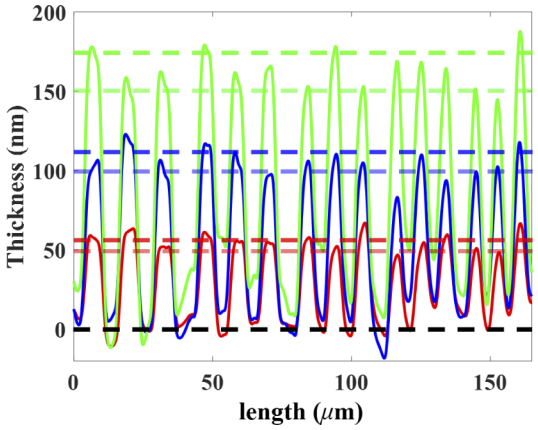

Fig. 6. Experimental validation of the proposed system for QPI of the thinnest USAF-type resolution tests of a Benchmark quantitative phase target. Red, blue, and green lines are 50, 100, and 150 nm thickness profiles, respectively. Upper and lower color-coded dashed lines mean estimated and nominal values provided by manufacturer for each thickness, respectively.

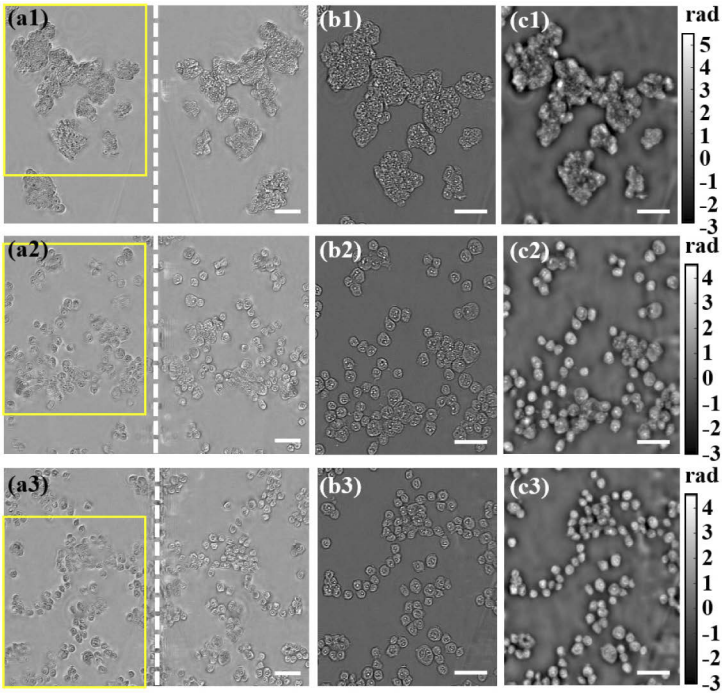

Fig. 7. Experimental results conducted on static biosamples: (1), (2), and (3) rows include LNCAP, PC-3, and RWPE-1 cell lines, respectively. Each column includes: (a) full-frame normalized image, (b) axial intensity derivative of the region enclosed in the yellow rectangle included in column (a), (c) phase map provided by our system. White scale bars are 50 µm.

3.5. Experimental validation for dynamic samples

And finally, in order to validate our approach from a single-shot perspective, we have carried out an additional experiment involving living human sperm cells. The sperm cells have approximately

Optics EXPRESS

a head's length and width of 4 and 5 μm, respectively, a total length of 45 μm and a tail's width below 1 μm. The sperm cells are swimming into the proper semen without a dilution process and the sample is inserted by micro pipetting into a counting chamber (10 μm thickness). In order to have a higher frame rate, we have replaced the previous digital sensor by a different one (Ximea Model MQ042CG-CM, 2048 × 2048, 5.5 μm, 90 fps full frame) with higher recording speed. The experimental results are presented in Visualization 1, in which (a) and (b) include the sequence of the recorded negative- and positive-defocused intensity images, respectively, and (c) shows the retrieved quantitative phase images. Figure 8 includes the first frame of the whole video sequence (Visualization 1).

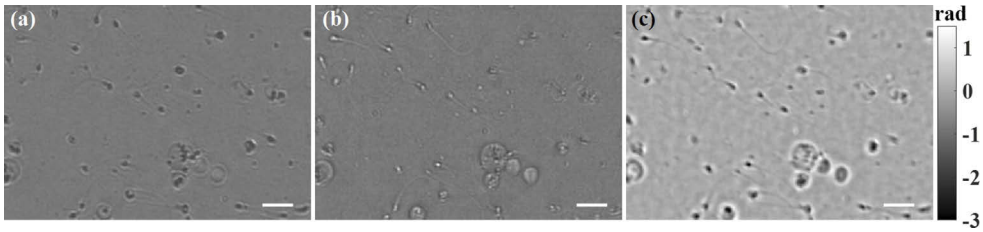

Fig. 8. First frame of the experimental results conducted on dynamic sperm cells (Visualization 1): (a), and (b) negative- and positive-defocused intensity images, respectively, and (c) retrieved phase image. White scale bars are 20 μm.

4. Discussion and conclusions

In this contribution, we have reported on a low-cost, simple, and robust single-shot TIE-based optical module which can be implemented at the output port of any microscope. Essentially, the module includes three optical elements having different roles: 1) a BSC placed in a non-conventional way for the simultaneous recording of two laterally shifted and inverted intensity images (field of view multiplexing approach); 2) a labmade SL for astigmatism compensation caused by specific position of the BSC; and 3) an OG plate with a given thickness for inducing the adequate negative- and positive-defocusing between the two replicas (single-shot TIE algorithm implementation). The two defocused replicas provided by the novel system are numerically processed for spatial adjustment each other, and then utilized for axial derivative estimation. Finally, quantitative phase retrieval is carried out by solving the TIE (see Eq. (9)).

We have also presented a complete description and analysis of the system starting from calibration purposes to dynamic biosample validation. First, a phase resolution test target is used to show the whole process step by step regarding the proposed TIE-based approach, including axial defocusing distance calibration as well as QPI validation. Second, the experimental results achieved for the case of prostate cancer cells demonstrate the potential of the proposed system for QPI of biomedical fixed samples. And finally, flowing sperm cells validate the proposed method for the characterization of dynamic biosamples.

The proposed optical module has pros and cons when is compared with other existing single-shot TIE-based QPI methods. Regarding the advantages, since the proposed method only use a single digital sensor, it compares favourably in terms of cost-effectiveness with the recently proposed method by Chen *et al.* [50] and other methods using several digital sensors [40], spatial light modulators [38,41], or electrically tunable lenses [37]. In addition, the simultaneous use of several electronic devices can lead to problems in synchronization between them to record the same instantaneous frame, something especially relevant when dealing with high frame rates because the sample is moving fast (dynamic/live sample imaging). Furthermore, although the methods based on high-order TIE [34,49] provides a more accurate QPI, they need multiple defocused images, which inevitably complicates the imaging system and restrict much

Optics EXPRESS

more the FOV than our method. Something similar happens with the approaches based on the recording of three laterally separated images by a single camera [41,42]. Moreover, although Nomura *et al.* proposed a smart method in which only an OG plate was employed to provide both replication and defocusing between images [46], our method compares favourably in the sense that it does not require to introduce a diaphragm to restrict the extension of each image to avoid overlapping between the replicas. As in lateral shearing interferometry where coherence overlapping is pursued [66], the lateral separation of the two images is a function of the plate thickness, its refractive index value and the angle of incidence. However, we are not interested in the overlapping both images because interference is not the underlaying principles when thinking in terms of TIE-based reconstruction. Thus, large image separation needs either high plate thickness, so the defocus between replicas will be also very different, or spatial image restriction by using diaphragms, thus reducing a lot the useful FOV. In addition, that method [46] may present astigmatism problems due to the use of a tilted plane-parallel plate [67]. By contrast, in our method, the astigmatism is well compensated with the use of a SL. Also, our method does not require of sophisticated/complex optical components or systems, such as microfluidic systems [36], Greek-ladder sieves [47], or dielectric metasurfaces [48]. Finally, our method requires of neither high coherence light sources nor sparse samples unlike [44].

The main drawbacks of the proposed method are the FOV reduction required for the recording of two defocus images in a single frame, and practical troubles coming from the correct alignment and tunning of the optical elements (especially the SL and object illumination) which can impact in deteriorate the quality of the reconstructed phase images. Also, the optimum defocus distance, that is, the optimum OG plate thickness, is different when considering a different microscope objective with a different magnification (see Eqs. (3) and (4)); thus, a set of OG plates with different thicknesses is needed for using the proposed module when interchanging the objectives in the microscope revolving nosepiece. In addition, the proposed method may be penalized from an aberration point of view when dealing with polychromatic light sources.

Although the proposed method has been validated for a microscopy system in an optical table, the layout could be also assembled into a compact and portable add-on module, which could be attached at the output port of any (upright or inverted) conventional microscope in future works. Those possibilities could expand the applicability of our approach in different areas of biomedicine such as microfluidics, sperm assessment, or cell-drug interaction among others, being especially promising for living cell/tissue culture investigations due to its single snapshot operational principle.

Funding. Spanish Ministerio de Economía, Industria y Competitividad and Fondo Europeo de Desarrollo Regional under the project FIS2017-89748-P.

Disclosures. The authors declare that there are no conflicts of interest related to this article.

Data availability. Data underlying the results presented in this paper are not publicly available at this time but may be obtained from the authors upon reasonable request.

References

1. F. Zernike, "Phase contrast, a new method for the microscopic observation of transparent objects," Physica **9**(7), 686–698 (1942).
2. M. Pluta, *Advanced Light Microscopy* (Elsevier, 1989).
3. M. R. Arnison, K. G. Larkin, C. J. R. Sheppard, N. I. Smith, and C. J. Cogswell, "Linear phase imaging using differential interference contrast microscopy," J. Microsc. **214**(1), 7–12 (2004).
4. S. V. King, A. Libertun, R. Piestun, C. J. Cogswell, and C. Preza, "Quantitative phase microscopy through differential interference imaging," J. Biomed. Opt. **13**(2), 024020 (2008).
5. S. S. Kou, L. Waller, G. Barbastathis, and C. J. R. Sheppard, "Transport-of-intensity approach to differential interference contrast (TI-DIC) microscopy for quantitative phase imaging," Opt. Lett. **35**(3), 447 (2010).
6. P. Gao, B. Yao, I. Harder, N. Lindlein, and F. J. Torcal-Milla, "Phase-shifting Zernike phase contrast microscopy for quantitative phase measurement," Opt. Lett. **36**(21), 4305 (2011).
7. G. Popescu, *Quantitative Phase Imaging of Cells and Tissues* (McGraw-Hill, 2011).

Optics EXPRESS

8. Y. K. Park, C. Depeursinge, and G. Popescu, "Quantitative phase imaging in biomedicine," Nat. Photonics **12**(10), 578–589 (2018).
9. C. Zuo, J. Li, J. Sun, Y. Fan, J. Zhang, L. Lu, R. Zhang, B. Wang, L. Huang, and Q. Chen, "Transport of intensity equation: a tutorial," Opt. Lasers Eng. **135**, 106187 (2020).
10. P. Marquet, B. Rappaz, P. J. Magistretti, E. Cuche, Y. Emery, T. Colomb, and C. Depeursinge, "Digital holographic microscopy: a noninvasive contrast imaging technique allowing quantitative visualization of living cells with subwavelength axial accuracy," Opt. Lett. **30**(5), 468 (2005).
11. B. Kemper and G. von Bally, "Digital holographic microscopy for live cell applications and technical inspection," Appl. Opt. **47**(4), A52 (2008).
12. M. K. Kim, *Digital Holographic Microscopy. Principles, Techniques, and Applications* (Springer US, 2011).
13. B. C. Platt and R. Shack, "History and principles of Shack-Hartmann wavefront sensing," J. Refract. Surg. **17**(5), 573 (2001).
14. R. Ragazzoni, "Pupil plane wavefront sensing with an oscillating prism," J. Mod. Opt. **43**(2), 289–293 (1996).
15. R. W. Gerchberg and W. O. Saxton, "A practical algorithm for the determination of phase from image and diffraction plane pictures," Optik (Stuttg **35**, 237–246 (1972).
16. H. M. L. Faulkner and J. M. Rodenburg, "Movable aperture lensless transmission microscopy: a novel phase retrieval algorithm," Phys. Rev. Lett. **93**(2), 023903 (2004).
17. G. Zheng, R. Horstmeyer, and C. Yang, "Wide-field, high-resolution Fourier ptychographic microscopy," Nat. Photonics **7**(9), 739–745 (2013).
18. M. R. Teague, "Deterministic phase retrieval: a Green's function solution," J. Opt. Soc. Am. **73**(11), 1434–1441 (1983).
19. D. Paganin and K. A. Nugent, "Noninterferometric phase imaging with partially coherent light," Phys. Rev. Lett. **80**(12), 2586–2589 (1998).
20. C. J. R. Sheppard and S. B. Mehta, "Quantitative phase-gradient imaging at high resolution with asymmetric illumination-based differential phase contrast," Opt. Lett. **34**(13), 1924–1926 (2009).
21. D. Lee, S. Ryu, U. Kim, D. Jung, and C. Joo, "Color-coded LED microscopy for multi-contrast and quantitative phase-gradient imaging," Biomed. Opt. Express **6**(12), 4912–4922 (2015).
22. L. Waller and L. Tian, "Quantitative differential phase contrast imaging in an LED array microscope," Opt. Express **23**(9), 11394–11403 (2015).
23. M. R. Teague, "Irradiance moments: their propagation and use for unique retrieval of phase," J. Opt. Soc. Am. **72**(9), 1199–1209 (1982).
24. N. Streibl, "Phase imaging by the transport equation of intensity," Opt. Commun. **49**(1), 6–10 (1984).
25. A. Barty, K. A. Nugent, D. Paganin, and A. Roberts, "Quantitative optical phase microscopy," Opt. Lett. **23**(11), 817 (1998).
26. A. Roberts, E. Ampem-Lassen, A. Barty, K. A. Nugent, G. W. Baxter, N. M. Dragomir, and S. T. Huntington, "Refractive-index profiling of optical fibers with axial symmetry by use of quantitative phase microscopy," Opt. Lett. **27**(23), 2061 (2002).
27. E. Ampem-Lassen, S. T. Huntington, N. M. Dragomir, K. A. Nugent, and A. Roberts, "Refractive index profiling of axially symmetric optical fibers: a new technique," Opt. Express **13**(9), 3277 (2005).
28. C. Dorrer and J. D. Zuegel, "Optical testing using the transport-of-intensity equation," Opt. Express **15**(12), 7165 (2007).
29. A. Darudi, R. Shomali, and M. T. Tavassoly, "Determination of the refractive index profile of a symmetric fiber preform by the transport of intensity equation," Opt. Laser Technol. **40**(6), 850–853 (2008).
30. C. L. Curl, C. J. Bellair, P. J. Harris, B. E. Allman, A. Roberts, K. A. Nugent, and L. M. D. Delbridge, "Quantitative phase microscopy: A new tool for investigating the structure and function of unstained live cells," Clin. Exp. Pharmacol. Physiol. **31**(12), 896–901 (2004).
31. C. L. Curl, C. J. Bellair, P. J. Harris, B. E. Allman, A. Roberts, K. A. Nugent, and L. M. D. Delbridge, "Single cell volume measurement by quantitative phase microscopy (QPM): A case study of erythrocyte morphology," Cell. Physiol. Biochem. **17**(5-6), 193–200 (2006).
32. G. J. Ross, A. W. Bigelow, G. Randers-Pehrson, C. C. Peng, and D. J. Brenner, "Phase-based cell imaging techniques for microbeam irradiations," Nucl. Instruments Methods Phys. Res. Sect. B Beam Interact. with Mater. Atoms **241**(1-4), 387–391 (2005).
33. N. M. Dragomir, X. M. Goh, C. L. Curl, L. M. D. Delbridge, and A. Roberts, "Quantitative polarized phase microscopy for birefringence imaging," Opt. Express **15**(26), 17690 (2007).
34. L. Waller, Y. Luo, S. Y. Yang, and G. Barbastathis, "Transport of intensity phase imaging in a volume holographic microscope," Opt. Lett. **35**(17), 2961–2963 (2010).
35. L. Waller, S. S. Kou, C. J. R. Sheppard, and G. Barbastathis, "Phase from chromatic aberrations," Opt. Express **18**(22), 22817 (2010).
36. S. S. Gorthi and E. Schonbrun, "Phase imaging flow cytometry using a focus-stack collecting microscopeope," Opt. Lett. **37**(4), 707–709 (2012).
37. C. Zuo, Q. Chen, W. Qu, and A. Asundi, "High-speed transport-of-intensity phase microscopy with an electrically tunable lens," Opt. Express **21**(20), 24060 (2013).

Optics EXPRESS

38. C. Zuo, Q. Chen, W. Qu, and A. Asundi, "Noninterferometric single-shot quantitative phase microscopy," Opt. Lett. **38**(18), 3538 (2013).
39. J. M. Di Martino, G. A. Ayubi, E. A. Dalchiele, J. R. Alonso, A. Fernández, J. L. Flores, C. D. Perciante, and J. A. Ferrari, "Single-shot phase recovery using two laterally separated defocused images," Opt. Commun. **293**, 1–3 (2013).
40. X. Tian, W. Yu, X. Meng, A. Sun, L. Xue, C. Liu, and S. Wang, "Real-time quantitative phase imaging based on transport of intensity equation with dual simultaneously recorded field of view," Opt. Lett. **41**(7), 1427 (2016).
41. W. Yu, X. Tian, X. He, X. Song, L. Xue, C. Liu, and S. Wang, "Real time quantitative phase microscopy based on single-shot transport of intensity equation (ssTIE) method," Appl. Phys. Lett. **109**(7), 071112 (2016).
42. Z. Yang and Q. Zhan, "Single-Shot Smartphone-Based Quantitative Phase Imaging Using a Distorted Grating," PLoS One **11**(7), e0159596 (2016).
43. Y. Li, J. Di, C. Ma, J. Zhang, J. Zhong, K. Wang, T. Xi, and J. Zhao, "Quantitative phase microscopy for cellular dynamics based on transport of intensity equation," Opt. Express **26**(1), 593 (2018).
44. W.-J. Zhou, X. Guan, F. Liu, Y. Yu, H. Zhang, T.-C. Poon, and P. P. Banerjee, "Phase retrieval based on transport of intensity and digital holography," Appl. Opt. **57**, A234 (2018).
45. A. K. Gupta, R. Mahendra, and N. K. Nishchal, "Single-shot phase imaging based on transport of intensity equation," Opt. Commun. **477**, 126347 (2020).
46. T. Nomura, K. Komuro, N. Yoneda, S. Kakei, A. Onishi, and Y. Saita, "Phase imaging based on Scan-less transport of intensity equation (Conference Presentation)," Proc. SPIE **11402**, 114020H (2020).
47. X. Zhang, S. Yang, Y. Li, J. Zhang, G. Zheng, Y. Zhang, S. Zhou, and J. Zhu, "Single-shot common-path transport of intensity equation method with Greek-ladder sieves," Opt. Lasers Eng. **126**, 105898 (2020).
48. E. Engay, D. Huo, R. Malureanu, A.-I. Bunea, and A. Lavrinenko, "Polarization-Dependent All-Dielectric Metasurface for Single-Shot Quantitative Phase Imaging," Nano Lett. **21**(9), 3820–3826 (2021).
49. N. Yoneda, A. Onishi, Y. Saita, K. Komuro, and T. Nomura, "Single-shot higher-order transport-of-intensity quantitative phase imaging based on computer-generated holography," Opt. Express **29**(4), 4783–4801 (2021).
50. C. Chen, Y.-N. Lu, H. Huang, K. Yan, Z. Jiang, X. He, Y. Kong, C. Liu, F. Liu, L. Xue, and S. Wang, "PhaseRMiC: phase real-time microscope camera for live cell imaging," Biomed. Opt. Express **12**(8), 5261–5271 (2021).
51. J. A. Picazo-Bueno, M. Trusiak, and V. Micó, "Single-shot slightly off-axis digital holographic microscopy with add-on module based on beamsplitter cube," Opt. Express **27**(4), 5655 (2019).
52. M. Trusiak, J.-A. Picazo-Bueno, K. Patorski, P. Zdańkowski, and V. Mico, "Single-shot two-frame π-shifted spatially multiplexed interference phase microscopy," J. Biomed. Opt. **24**(09), 1 (2019).
53. E. Acosta and J. Arines, "Low-cost adaptive astigmatism compensator for improvement of eye fundus camera," Opt. Lett. **36**(21), 4164–4166 (2011).
54. J. Arines and E. Acosta, "Adaptive astigmatism-correcting device for eyepieces," Optom. Vis. Sci. **88**(12), 1524–1528 (2011).
55. T. Colomb, E. Cuche, F. Charrière, J. Kühn, N. Aspert, F. Montfort, P. Marquet, and C. Depeursinge, "Automatic procedure for aberration compensation in digital holographic microscopy and applications to specimen shape compensation," Appl. Opt. **45**(5), 851–863 (2006).
56. T. E. Gureyev and K. A. Nugent, "Rapid quantitative phase imaging using the transport of intensity equation," Opt. Commun. **133**(1-6), 339–346 (1997).
57. L. J. Allen and M. P. Oxley, "Phase retrieval from series of images obtained by defocus variation," Opt. Commun. **199**(1-4), 65–75 (2001).
58. K. Ishizuka and B. Allman, "Phase measurement of atomic resolution image using transport of intensity equation," J. Electron Microsc. (Tokyo **54**(3), 191–197 (2005).
59. L. Tian, J. C. Petruccelli, and G. Barbastathis, "Nonlinear diffusion regularization for transport of intensity phase imaging," Opt. Lett. **37**(19), 4131 (2012).
60. C. Zuo, Q. Chen, W. Qu, and A. Asundi, "Direct continuous phase demodulation in digital holography with use of the transport-of-intensity equation," Opt. Commun. **309**, 221–226 (2013).
61. D. Paganin, A. Barty, P. J. Mcmahon, and K. A. Nugent, "Quantitative phase-amplitude microscopy. III. The effects of noise," J. Microsc. **214**(1), 51–61 (2004).
62. A. V. Martin, F. R. Chen, W. K. Hsieh, J. J. Kai, S. D. Findlay, and L. J. Allen, "Spatial incoherence in phase retrieval based on focus variation," Ultramicroscopy **106**(10), 914–924 (2006).
63. E. D. Barone-Nugent, A. Barty, and K. A. Nugent, "Quantitative phase-amplitude microscopy I: optical microscopy," J. Microsc. **206**(3), 194–203 (2002).
64. M. Beleggia, M. A. Schofield, V. V. Volkov, and Y. Zhu, "On the transport of intensity technique for phase retrieval," Ultramicroscopy **102**(1), 37–49 (2004).
65. G. Barbastathis, L. Waller, and L. Tian, "Transport of Intensity phase-amplitude imaging with higher order intensity derivatives," Opt. Express **18**(12), 12552–12561 (2010).
66. K.-B. Seo, B.-M. Kim, and E.-S. Kim, "Digital holographic microscopy based on a modified lateral shearing interferometer for three-dimensional visual inspection of nanoscale defects on transparent objects," Nanoscale Res. Lett. **9**(1), 1–14 (2014).
67. J. Braat, "Analytical expressions for the wave-front aberration coefficients of a tilted plane-parallel plate," Appl. Opt. **36**(32), 8459–8467 (1997).